Research Article | Vol. 24, No. 22 | 31 Oct 2016 | OPTICS EXPRESS A1360

Optics EXPRESS

Experimental and numerical characterization of a new 45 kW_{el} multisource high-flux solar simulator

GAËL LEVÊQUE,[1] ROMAN BADER,[2] WOJCIECH LIPIŃSKI,[2,3] AND SOPHIA HAUSSENER,[1,4]

[1]*Ecole Polytechnique Fédérale de Lausanne (EPFL), Laboratory of Renewable Energy Science and Engineering. 1015 Lausanne, Switzerland*
[2]*Research School of Engineering, The Australian National University, Canberra ACT 2601, Australia*
[3]*wojciech.lipinski@anu.edu.au*
[4]*sophia.haussener@epfl.ch*

Abstract: The performance of a new high-flux solar simulator consisting of 18 × 2.5 kW_{el} radiation modules has been evaluated. Grayscale images of the radiative flux distribution at the focus are acquired for each module individually using a water-cooled Lambertian target plate and a CCD camera. Raw images are corrected for dark current, normalized by the exposure time and calibrated with local absolute heat flux measurements to produce radiative flux maps with 180 µm resolution. The resulting measured peak flux is 1.0–1.5 ± 0.2 MW m^{-2} per radiation module and 21.7 ± 2 MW m^{-2} for the sum of all 18 radiation modules. Integrating the flux distribution for all 18 radiation modules over a circular area of 5 cm diameter yields a mean radiative flux of 3.8 MW m^{-2} and an incident radiative power of 7.5 kW. A Monte Carlo ray-tracing simulation of the simulator is calibrated with the experimental results. The agreement between experimental and numerical results is characterized in terms of a 4.2% difference in peak flux and correlation coefficients of 0.9990 and 0.9995 for the local and mean radial flux profiles, respectively. The best-fit simulation parameters include the lamp efficiency of 39.4% and the mirror surface error of 0.85 mrad.

OCIS codes: (350.6050) Solar energy; (230.6080) Sources.

References and links

1. R. Bader and W. Lipiński, "Thermochemical processes," in *Solar Energy*, G.M. Crawley (World Scientific Publishing, 2016).
2. C. Graves, S. D. Ebbesen, M. Mogensen, and K. S. Lackner, "Sustainable hydrocarbon fuels by recycling CO_2 and H_2 O with renewable or nuclear energy," Renew. Sustain. Energy Rev. **15**(1), 1–23 (2011).
3. S. Rodat, S. Abanades, and G. Flamant, "Co-production of hydrogen and carbon black from solar thermal methane splitting in a tubular reactor prototype," Sol. Energy **85**(4), 645–652 (2011).
4. A. Meier and A. Steinfeld, "Solar Energy in Thermochemical Processing," in *Solar Energy*, C. Richter, D. Lincot, and C. A. Gueymard, eds. (Springer New York, 2013), pp. 521–552.
5. G. Lêveque and S. Abanades, "Thermodynamic and kinetic study of the carbothermal reduction of SnO_2 for solar thermochemical fuel generation," Energy Fuels **28**, 1396 (2013).
6. G. Levêque and S. Abanades, "Investigation of thermal and carbothermal reduction of volatile oxides (ZnO, SnO_2, GeO_2, and MgO) via solar-driven vacuum thermogravimetry for thermochemical production of solar fuels," Thermochim. Acta **605**, 86–94 (2015).
7. A. Meier, E. Bonaldi, G. M. Cella, W. Lipiński, and D. Wuillemin, "Solar chemical reactor technology for industrial production of lime," Sol. Energy **80**(10), 1355–1362 (2006).
8. V. Augugliaro, A. Lauricella, L. Rizzuti, M. Schiavello, and A. Sclafani, "Conversion of solar energy to chemical energy by photoassisted processes—I. Preliminary results on ammonia production over doped titanium dioxide catalysts in a fluidized bed reactor," Int. J. Hydrogen Energy **7**(11), 845–849 (1982).
9. R. Bader, S. Haussener, and W. Lipiński, "Optical design of multisource high-flux solar simulators," J. Sol. Energy Eng. **137**(2), 21012 (2014).
10. G. Olalde, "Final report - SOLFACE," Project report CORDIS, (2007).
11. R. Bader, L. Schmidt, S. Haussener, and W. Lipinski, "A 45 kWe multi-source high-flux solar simulator," in *Light, Energy and the Environment*, OSA Technical Digest (online) (Optical Society of America, 2014), paper RW4B.4. R.

#268581 http://dx.doi.org/10.1364/OE.24.0A1360
Journal © 2016 Received 17 Jun 2016; revised 11 Aug 2016; accepted 11 Aug 2016; published 16 Sep 2016

Optics EXPRESS

12. K. Lovegrove, G. Burgess, and J. Pye, "A new 500m^2 paraboloidal dish solar concentrator," Sol. Energy **85**(4), 620–626 (2011).
13. K. R. Krueger, W. Lipiński, and J. H. Davidson, "Operational performance of the University of Minnesota 45 kW$_e$ high-flux solar simulator," J. Sol. Energy Eng. **135**(4), 044501 (2013).
14. J. Sarwar, G. Georgakis, R. LaChance, and N. Ozalp, "Description and characterization of an adjustable flux solar simulator for solar thermal, thermochemical and photovoltaic applications," Sol. Energy **100**, 179–194 (2014).
15. S. Ulmer, W. Reinalter, P. Heller, E. Lüpfert, and D. Martínez, "Beam characterization and improvement with a flux mapping system for dish concentrators," J. Sol. Energy Eng. **124**(2), 182 (2002).
16. J. Petrasch, P. Coray, A. Meier, M. Brack, P. Häberling, D. Wuillemin, and A. Steinfeld, "A novel 50 kW 11,000 suns high-flux solar simulator based on an array of xenon arc lamps," J. Sol. Energy Eng. **129**(4), 405 (2007).
17. X. Dong, Z. Sun, G. J. Nathan, P. J. Ashman, and D. Gu, "Time-resolved spectra of solar simulators employing metal halide and xenon arc lamps," Sol. Energy **115**, 613–620 (2015).
18. A. Rabl, *Active Solar Collectors and Their Applications* (Oxford University Press, 1985).
19. J. Ballestrín, M. Rodríguez-Alonso, J. Rodríguez, I. Cañadas, F. J. Barbero, L. W. Langley, and A. Barnes, "Calibration of high-heat-flux sensors in a solar furnace," Metrologia **43**(6), 495–500 (2006).
20. K. R. Krueger, J. H. Davidson, and W. Lipiński, "Design of a new 45 kW$_e$ high-flux solar simulator for high-temperature solar thermal and thermochemical research," J. Sol. Energy Eng. **133**(1), 011013 (2011).
21. R. Gill, E. Bush, P. Haueter, and P. Loutzenhiser, "Characterization of a 6 kW high-flux solar simulator with an array of xenon arc lamps capable of concentrations of nearly 5000 suns," Rev. Sci. Instrum. **86**(12), 125107 (2015).
22. E. Guillot, I. Alxneit, J. Ballestrin, J. L. Sans, and C. Willsh, "Comparison of 3 heat flux gauges and a water calorimeter for concentrated solar irradiance measurement," Energy Procedia **49**, 2090–2099 (2014).
23. D. Nakar, A. Malul, D. Feuermann, and J. M. Gordon, "Radiometric characterization of ultrahigh radiance xenon short-arc discharge lamps," Appl. Opt. **47**(2), 224–229 (2008).
24. K. R. Krueger, "Design and characterization of a concentrating solar simulator," University of Minnesota (2012).

1. Introduction

Concentrated solar radiation is a high-exergy source of energy, suitable for efficient production of electricity, fuels, and commodity materials [1]. There is a growing interest in research dealing with solar thermochemical processes to produce fuels such as hydrogen, synthesis gas and liquid hydrocarbons [2–5], and commodity materials such as metals [6], lime [7], and ammonia [8]. Research and development of high-temperature solar systems require stable and controlled experimental conditions for reproducible high-flux testing of materials, receivers, and reactor prototypes. High-flux solar simulators (HFSS) mimicking radiative characteristics of typical point focusing solar concentrators have been deployed to allow for testing under controlled laboratory conditions. They concentrate the emitted radiation on a small focal target area, corresponding to an aperture of cavity-type receivers that capture and convert the incident radiation. The characteristics of the high-flux radiative output significantly differ from those obtained with line or large focal target area focusing simulators. The multisource HFSS radiative characteristics depend on the type, power and geometry of the artificial light sources, and the geometry and quality of the reflectors used. The majority of the existing HFSS facilities use between 1 and 10 high-intensity xenon short-arc lamps coupled to ellipsoidal reflectors [9]. The spectra of Xe short-arc lamps show similarities with that of natural terrestrial solar radiation as discussed in Bader et al. [9]. The power levels of the lamps used in multisource HFSSs range from ~6 to 15 kW$_{el}$. Existing HFSSs deliver ~1 to 20 kW of radiative power onto a 60-mm-diameter target area. Reported peak fluxes are between 3.8 and 16 MW m^{-2} [9]. These values can be compared to the highest claimed values for an actual solar furnace, with 1.5 kW of solar energy and a peak flux of 16 MW m^{-2} for a 2 m^2 parabola [10].

Optics EXPRESS

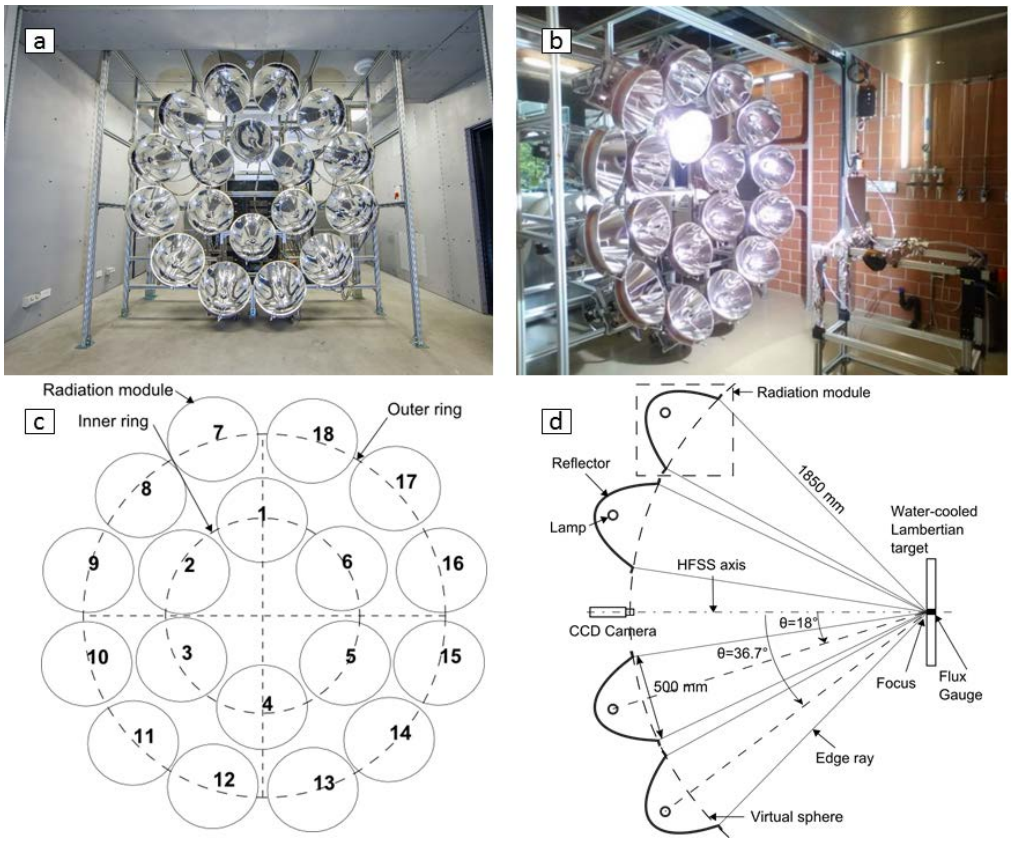

Fig. 1. 45 kW_{el} high-flux solar simulator facility consisting of 18 radiation modules arranged in two concentric rings: photographs of the completed facilities at ANU (a) and École Polytechnique Fédérale de Lausanne (b), reference numbering of the radiation modules (c), and schematic cross-section of the HFSS, CCD camera, and water-cooled Lambertian target (d). CCD camera and target are positioned coaxially with the HFSS.

A new 45 kW_{el} multisource HFSS has recently been designed, followed by construction of two devices at the Australian National University and at Ecole Polytechnique Fédérale de Lausanne, as shown in Fig. 1 [9,11]. The design consists of 18 × 2.5 kW_{el} radiation modules arranged over the surface of a virtual sphere of 1933 mm radius (measured from the lamp position). Compared to existing HFSSs, an increased number of radiation modules is used to achieve a more uniform angular radiation distribution, more closely approximating the typical radiative characteristics of an actual parabolic solar dish concentrator, i.e. an axi-symmetric distribution and a rim angle of 45° [9,12]. This reduces the risk of local radiative flux peaks ("hot spots") and hence high thermo-mechanical stresses and strains on surfaces behind the focal plane (e.g. cavity receiver walls). A larger number of radiation modules further allows for a finer adjustment of the radiative power output and a lower minimum power level. In addition, the smaller reflectors used in the present design can be manufactured via electroforming, as opposed to metal spinning used for previous HFSSs, resulting in substantially improved reflector quality and, consequently, higher optical efficiencies.

This paper describes the evaluation of the operational performance of this new HFSS. The methodologies to calibrate and characterize the HFSS are detailed, and experimental and numerical results are presented. The experimental results reported are obtained with the setup at EPFL.

Optics EXPRESS

2. Methods

To measure the flux distribution produced by the array of radiation modules at the focus of the HFSS, we follow the common approach described in [13,14], which uses a diffusively reflecting (Lambertian) flat target plate, a CCD (charge-coupled device) camera, and a heat flux gauge. This approach is based on four assumptions, elaborated in the following sections: (*i*) the radiative flux is additive, i.e. the flux map resulting from any number of radiation modules equals the sum of the flux maps of the individual modules; (*ii*) calibration of the flux gauge is adapted to the spectrum of the light source; (*iii*) the radiation spectrum is uniform over the target area; and (*iv*) the CCD camera's response is linear and uniform with respect to the incident radiative flux and position on the chip.

2.1. Experimental setup and procedures

The radiative flux measurement system is shown schematically in Fig. 1(d). Grayscale (GS) images of the Lambertian target (Haueter Engineering GmbH, 350 × 350 mm, water-cooled aluminum body, plasma spray-coated with alumina) at the focal plane are taken for each radiation module individually, using a CCD camera (Basler scA 1400-17 gm, 1.5 MP, 12 bit pixel depth) mounted with a manual zoom lens (Computar M6Z1212, f = 12.5–75 mm, Fujinon HE20-1 2 × extender) with a neutral density filter (Midwest ND400, optical density 4). This choice of camera and lens leads to a resolution of the target surface at the focal plane of 0.18 mm. As indicated in Fig. 1(d), the arrangement of the radiation modules allows positioning of the camera coaxially with the HFSS, avoiding the need for a geometric transformation of the raw images [15,16]. The GS live images are first used to manually adjust the orientation of each radiation module and the position of the lamp relative to the reflector, to maximize the radiative flux at the focus. The positioning accuracy is limited by the precision of the manual adjustment: moving the peak by 1 mm requires module rotation by 0.03°. The dark current of the CCD camera is measured using non-exposed images. Heat flux measurements are taken at the focal plane with an absolute heat flux gauge (Vatell Corporation, TG1000-0, colloidal graphite coated, range 0–10 MW m^{-2}, active area 1.82 mm^2, repeatability < 3%) and compared to GS images to establish a GS–radiative flux relationship. This relationship allows producing absolute flux maps from GS images. The total radiative flux distribution of all 18 radiation modules is obtained by superimposing the results for the individual modules. In addition to the flux measurements at the focal plane of the HFSS, flux distributions are measured in various planes perpendicular to the optical axis of the HFSS behind the focal plane, to analyze the flux uniformity. In this respect, the Lambertian target was positioned along the HFSS axis by installing it on a 3-D orthogonal coordinate table (Haueter Engineering GmbH, positioning precision 0.1 mm). The table was precisely positioned and leveled relative to the HFSS using a laser tool. The Lambertian target is oriented perpendicularly to the main axis of the 3-D coordinate table and the main axis of the 3-D coordinate table is aligned parallel to the HFSS axis.

2.2. Data acquisition and processing

A Labview interface has been developed to control the camera parameters, record images and flux measurement data, and monitor key temperature values. Flux images are composed of an average of 30 single images of the target, captured after the lamps have reached a steady output (i.e. intensity variation < 5%), usually taking about 10 minutes, in order to account for the presence of small fluctuations of the lamp output (a 300 Hz oscillation with an amplitude corresponding to 9% of the peak intensity has been reported [17]). The camera exposure time is selected such that the peak GS value is about 2/3 to 3/4 of the full-scale value, in order to maximize the brightness range of the images while avoiding overexposure. The same exposure time (t_{exp} = 150 ms) is used for all GS images recorded with the target at the focal plane and one radiation module in operation. Measurements in planes behind the focal plane

Optics EXPRESS

require an adjustment of the exposure time, varing between 200 and 600 ms. After averaging and dark current subtraction (measured dark current I_{dc} = 16 GS for all conditions), the GS image is normalized by the exposure time. The GS value of pixel (i, j) of the final image can be represented by:

$$P(i,j) = \frac{1}{t_{exp}}\left[\left(\frac{1}{N}\sum_{n=1}^{N} p_n(i,j)\right) - I_{dc}\right], \quad (1)$$

where N is the number of images averaged, and $p_n(i, j)$ is the GS value of pixel (i, j) in the n^{th} image.

Heat flux measurements are acquired using a Gantner Qblox 104 datalogger. The voltage output signal is converted to MW m^{-2} using the manufacturer's linear calibration curve, which is NIST traceable. The flux gauge is positioned starting 1 cm away from the location of the peak flux, and measurements are taken along the radial direction every 0.5 to 1 cm. The reading is averaged over a period similar to that of the image acquisition equal to 30 times the exposure time plus 200 ms of latency between images for post-processing.

2.3. Flux map calibration

The calibration constant, K'', to convert recorded GS of the CCD camera pixels to heat flux (MW m^{-2}) is determined by comparing radiative flux measurements obtained with the flux gauge to GS measurements obtained with the CCD camera. Measurements with the flux gauge are performed at least twice with different radiation modules in operation and at different flux gauge positions with radial steps of 0.5 to 1 cm from the center of the flux distribution. At each flux gauge position, GS images of the flux gauge are taken with all lamps turned off, and a Labview-implemented function is used to identify the pixels of the image that cover the active area of the flux gauge. After completing the flux measurement with the flux gauge, the flux gauge is replaced with the Lambertian target, GS images of the target are acquired with the same combination of radiation modules in operation, and the GS recorded by the camera are numerically averaged over the area corresponding to the active area of the flux gauge. The calibration constant, K'', is then obtained from:

$$\dot{q}(x,y) = K''\left[\frac{1}{M}\sum_{i}\sum_{j} P(i,j)\right] \text{ for } (i,j) \in S_{active}, \quad (2)$$

where $P(i, j)$ is calculated according to Eq. (1), $\dot{q}(x, y)$ is the heat flux measured by the flux gauge at position (x, y) in the focal plane, S_{active} is the ensemble of pixels (i, j) in the image of the Lambertian target that cover the active area of the flux gauge, and M is the number of pixels constituting S_{active}. The resulting calibration constant, K'', is independent of the exposure time of the camera used to acquire the GS image, as long as the image is processed according to Eq. (1).

Repeating the calibration procedure several times using different combinations of radiation modules in operation, placing the flux gauge at different positions in the focal plane, and comparing flux gauge measurements with different GS images taken at different times and with different exposure times allows to verify the linearity of the measurement system, the sensitivity of the measurement system to spectral variations within the flux distribution, the temporal stability of the flux distribution, and the repeatability of the calibration method.

Optics EXPRESS

2.4. Monte Carlo ray-tracing model

A Monte Carlo ray-tracing model of the HFSS was described previously [9]. The reflectors are modeled specularly reflecting with reflectivity of 0.9, corresponding to the solar reflectance of pure polished aluminum [18]. Errors in the orientation of the reflector surface normal vector are modeled as randomly distributed over the reflector surface with a Rayleigh probability density function with mode θ_{m}. The directional radiation emission distribution of the lamp measured by the lamp manufacturer is used to determine the ray's direction of emission. In previous work, the light-emitting arc was modeled as a uniformly emitting cylindrical volume, conical or spherical surface, or combination of multiple spherical and cylindrical surfaces [17]. Here, the spatial emission distribution measured by the lamp manufacturer is utilized. Assuming the distribution to be axisymmetric, this data provides the axial brightness distribution of the arc and the radius of the emitting volume as a function of axial position along the arc, *z*. Because the radial emission profile is unknown, an exponential probability distribution function is assumed according to:

$$p(r) = \exp\left(\frac{\log 0.01}{r_{\mathrm{arc}}(z)} C_1 r\right), \tag{3}$$

where $r_{\mathrm{arc}}(z)$ is the radius of the arc and C_1 is a model fitting parameter. Radiation emission from outside the arc (e.g. from the electrodes) is omitted in this study.

2.5. Model calibration

The model is calibrated by comparing the simulated and measured radiative flux distributions obtained at the focal plane with all 18 lamps in operation. Due to the axial symmetry of the 2-D flux distribution (cf. section 3.5), the 1-D radial flux profile, $\dot{q}_{\mathrm{r,local}}(r)$, with peak at $r = 0$ is used in the model calibration. In addition, the mean radiative flux profile, $\dot{q}_{\mathrm{r,mean}}(r)$, is used, defined as the average radiative flux within the area of radius *r*.

The agreement between simulated and measured radial flux profiles is quantified. The relative difference of measured and simulated flux peaks is calculated according to:

$$\varepsilon_{\mathrm{peak}} = \frac{\left|\dot{q}^{\mathrm{meas}}_{\mathrm{r,local}}(r=0) - \dot{q}^{\mathrm{sim}}_{\mathrm{r,local}}(r=0)\right|}{\dot{q}^{\mathrm{meas}}_{\mathrm{r,local}}(r=0)}. \tag{4}$$

The correlation coefficient for the simulated and measured radial flux profiles is defined by:

$$R_{\mathrm{local}} = \frac{\sum_{i=1}^{n}\left(\dot{q}^{\mathrm{meas}}_{\mathrm{r,local}}(r_i) - \bar{\dot{q}}^{\mathrm{meas}}_{\mathrm{r,local}}\right)\left(\dot{q}^{\mathrm{sim}}_{\mathrm{r,local}}(r_i) - \bar{\dot{q}}^{\mathrm{sim}}_{\mathrm{r,local}}\right)}{\left[\sum_{i=1}^{n}\left(\dot{q}^{\mathrm{meas}}_{\mathrm{r,local}}(r_i) - \bar{\dot{q}}^{\mathrm{meas}}_{\mathrm{r,local}}\right)^2 \sum_{i=1}^{n}\left(\dot{q}^{\mathrm{sim}}_{\mathrm{r,local}}(r_i) - \bar{\dot{q}}^{\mathrm{sim}}_{\mathrm{r,local}}\right)^2\right]^{1/2}}. \tag{5}$$

$\dot{q}^{\mathrm{meas}}_{\mathrm{r,local}}(r_i)$ and $\dot{q}^{\mathrm{sim}}_{\mathrm{r,local}}(r_i)$ denote the measured and simulated radiative flux at radius r_i ($i = 1, 2, ..., n$), respectively, and $\bar{\dot{q}}^{\mathrm{meas}}_{\mathrm{r,local}}$ and $\bar{\dot{q}}^{\mathrm{sim}}_{\mathrm{r,local}}$ are their averages within the entire flux map from $r = 0$ to r_n = 70 mm. Analogously to Eq. (5), the correlation coefficient for $\dot{q}_{\mathrm{r,mean}}$, R_{mean}, is defined.

The unknown parameters in the ray-tracing model are the lamp efficiency, η_{lamp}, the mode of the mirror surface error distribution, θ_{m}, and the arc model parameter C_1 (Eq. (3)). The lamp efficiency is adjusted so that the simulated radiative power arriving at the focal plane matches the measured radiative power. The mode of the mirror surface error distribution is adjusted so that the simulated and measured flux peaks match.. The arc model parameter is

Optics EXPRESS

adjusted to maximize the correlation of the simulated and measured radial flux profiles. Samples of 10^6 rays per lamp are used in the simulation. This value has been determined in a convergence study that shows that $\dot{q}^{\mathrm{sim}}_{\mathrm{r,mean}}(r)$, for $r = 5,10,15,30$ mm, varies by less than 0.2% as the number of rays per sample is increased from 10^6 to 10^7.

3. Results and discussion

3.1. Focusing of radiation modules

In order to maximize the radiative flux at the focal plane, each radiation module was oriented and focused such that the flux peaks of all radiation modules are aimed as closely to each other as possible. Figure 2 shows the measured position of the flux peak of each radiation module after its manual adjustment. Point (0, 0) corresponds to the mean center. This graph emphasizes the difficulty of focusing all radiation modules onto the same point. A variability of ± 2 mm in *x* and *y* direction of the peaks is observed except for lamp 6 and 18 which have a larger error in *y* positioning (respectively + 2.5 mm and –4.2 mm).

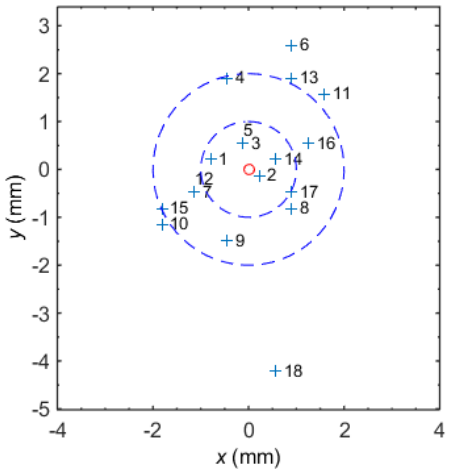

Fig. 2. Peak flux location for each of the 18 radiation modules (after manual orientation and focusing) on the flat target plate at the focal plane relative to the mean center (red circle). Dashed gray circles represent locations within 1 and 2 mm radius, respectively, measured from the mean center.

3.2. Determination of calibration constant

Several data points of measured radiative flux vs. average GS value obtained with different radiation module combinations, camera exposure times, and flux gauge positions are shown in Fig. 3. The results demonstrate the repeatability of the calibration and the linearity between normalized GS value and radiative flux. The results further verify that the normalization of the average GS value by the exposure time (cf. Equation (1)) allows to use the resulting calibration constant to calibrate images with different exposure times. In addition, spectral variations within the flux distribution do not appear to significantly affect the calculation of the calibration constant on the spatial domain considered (i.e. up to 150 mm away from the peak, the farthest position of the flux gauge).

The calibration constant determined for the present experimental setup is $K'' = 79 \pm 3$ kW m^{-2}(GS ms^{-1})$^{-1}$. The experimentally determined uncertainty of this parameter of 4% (confidence interval of 95%, Fig. 3) is consistent with the reported repeatability of the flux gauge of 3%. The difference between these two values is attributed to the positioning error of the table, of 0.1 mm (i.e. 0.56 pixel), and the discretization of the sensor's surface into pixels (exact sensor radius is 4.23 pixels). This translates into an uncertainty on the measured gray

Optics EXPRESS

scale which cannot be expressed simply because it depends on the local spatial variations of the flux. Nevertheless, it remains within the sensitivity range of the camera.

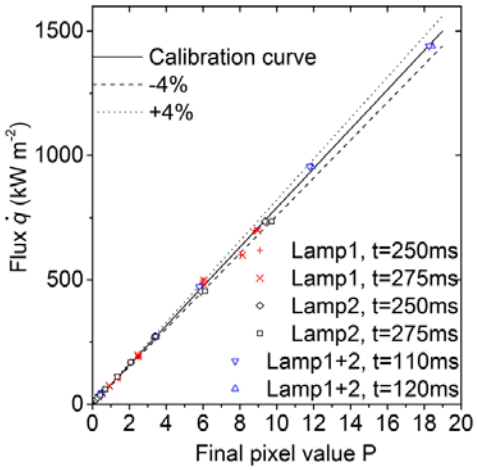

Fig. 3. Calibration curve comparing the flux measured by the flux gauge to the normalized GS value measured by the CCD camera at the same position as the flux gauge, for various flux gauge positions, lamps and lamp combinations, and camera exposure times. Each measurement point is an average over two consecutive measurements. The normalized GS values are corrected by the dark current value and the exposure time.

3.3. Validity of initial assumptions

3.3.1. Flux additivity

To verify the additivity of the flux maps of individual radiation modules (assumption *i*) in section 2), flux maps were acquired with sets of two radiation modules. The results are compared with the flux maps obtained by superimposing the flux maps obtained for the two individual radiation modules. Table 1 compares the results at selected positions within the flux map. The results show that the superposition of the individual flux maps of two radiation modules leads to the same result as the direct measurement of the flux map for the two radiation modules, within the repeatability of the flux gauge. These results confirm the validity of assumption *i*).

Table 1. Comparison of the radiative flux measured for sets of two radiation modules with the radiative flux obtained by superimposing the flux maps of the two individual lamps, for different lamp combinations and measurement locations.

Lamp	Position	Superposition (kW m^{-2})	Measured (kW m^{-2})	Error
1 & 2	1	2495	2526	**1%**
	2	1233	1203	**-3%**
	3	792	752	**-5%**
4 & 5	1	2836	2776	**-2%**
	2	2546	2495	**-2%**
	3	1223	1243	**2%**
	4	812	812	**0%**
5 & 6	1	2636	2646	**0%**
	2	2526	2596	**3%**
	3	1383	1363	**-1%**
	4	912	882	**-3%**
6 & 7	1	2756	2706	**-2%**
	2	2345	2345	**0%**
	3	1102	1082	**-2%**
	4	712	692	**-3%**

Optics EXPRESS

3.3.2. Suitability of flux gauge manufacturer's calibration for HFSS spectrum

The main source of errors observed in our measurements resulted from the calibration of the flux gauge. It was calibrated with a 1100 K blackbody, whose spectrum does not correspond to the spectrum delivered by the HFSS. Theoretically, this spectrum mismatch may lead to overestimation of the flux of over 30% [19]. In practice, a calorimetric method is often used to correct the calibration [20,21], even though such methods can introduce new error sources of similar order. To establish a common comparison ground for the various European laboratories involved in the SFERA project (Solar Facilities for the European Research Area), the degree of agreement between the different flux meters (both calorimeters and flux gauges) used in CNRS-PROMES (France), DLR (Germany), PSA-CIEMAT (Spain) and PSI (Switzerland) was studied [22]. This exhaustive study states that the flux gauge used in the present study, with manufacturer calibration, agrees to within 10% with absolute radiometers and calorimeters. Thus, a 10% uncertainty on the measured flux is estimated for our study.

3.3.3. Spatial uniformity of spectrum and linearity of CCD chip response

Though the linear relation between measured GS value and radiative flux shown in section 3.2 implies that both asumptions are correct, a more thorough study was performed. The hypotheses were checked by comparing pixel values measured at various locations with different exposure times. The results are shown in Fig. 4. The colors of the points correspond to the same pixel (each color is a different position on the target), each vertical group of points corresponds to the same image taken at a given exposure time. The chip linearly responds to the intensity of light, here adjusted with the exposure time (part one of assumption (*iv*)). This linear relation is the same, irrespective of the GS and coordinates of the pixel (all slopes have the same coefficient of $5.1 \times 10^{-3} \times GS_{t\text{exp} = 200\text{ms}}$), which supports assumption (*iii*) of a homogeneous spectrum over the target within the exposure times considered here, and the second part of assumption (*iv*) of an uniform chip response.

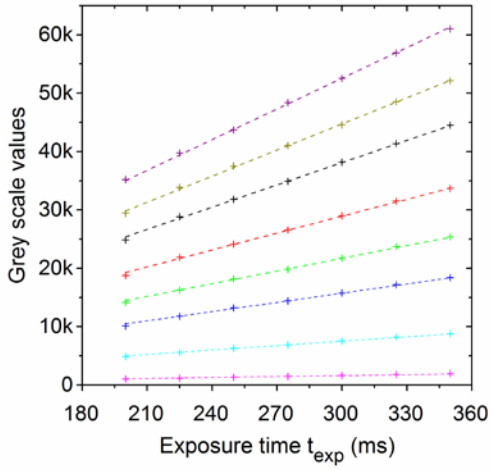

Fig. 4. Recorded GS value as a function of camera exposure time for different pixels (curves). All slopes have R^2>0.999.

3.4. Performance of individual radiation modules

Figure 5 shows the measured peak flux value for each radiation module. A variation of 49% is observed between lowest and hightest measured peak flux, with values ranging from 1020 to 1520 kW m^{-2}. This is attributed to axial positioning errors of the radiation modules relative to the target. To position the second focus of the radiation module (cf [9], Fig. 2) on a target point in the focal plane, the first focus would need to be positioned exactly at the distance

Optics EXPRESS

corresponding to the focal length of the reflector (1933 mm [9]) from the target point. The measured peak values remain unchanged after exchanging lamps (light bulbs) between radiation modules, which eliminates the lamp as the potential source of the variation in the measured peak fluxes.

In average, the radiation modules of the inner ring reach a higher peak flux than the radiation modules of the outer ring. This is explained by the difference in the incidence angle of the radiation beam on the target. The nominal incidence angle (relative to normal) of the center axis of the radiation module on the focal plane is θ = 18.0° ($\cos\theta$ = 0.951) for the radiation modules of the inner ring and 36.7° ($\cos\theta$ = 0.801) for the radiation modules of the outer ring.

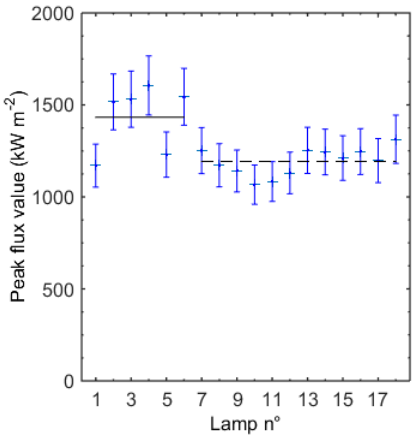

Fig. 5. Measured peak flux value and corresponding error bars (± 10%) for each radiation module. The plain gray line indicates the mean peak value for inner ring of lamps, and the dashed one for the outer ring (see Fig. 1).

3.5. Overall flux maps and radiative characteristics of the HFSS

The flux maps obtained for all individual radiation modules are superimposed to calculate the total output of the simulator with all 18 radiation modules in operation. The resulting radiative flux distribution at the focal plane is shown in Fig. 6(a). The flux map has a peak flux of 21.7 MW m^{-2} and shows a high degree of axial uniformity.

Figures 6(b)-6(d) show the flux maps obtained in planes parallel to the focal plane at distances of 2, 5 and 9 cm behind the focal plane. These results are used to evaluate the uniformity of the flux distribution on surfaces behind the focal plane, such as the walls of a cavity receiver or inside a volumetric receiver. Nonuniformities (“hot spots”) can lead to high local thermo-mechanical stresses that can lead to material damage and failure of the experimental setup. With increasing distance from the focal plane, the maximum radiative flux decreases rapidly, from 21.7 MW m^{-2} at the focal plane to 1.2 MW m^{-2} at 9 cm behind the focal plane. A flux pattern caused by the individual lamps can be observed, as well as slight asymmetries, which are attributed to be different levels of focusing of the individual lamps discussed in section 3.1, and slight mirror shape imperfections. Considering a disk-shaped target with 50 mm radius, the power measured in the focal plane and 9 cm behind the focal plane is 11.3 kW and 5.7 kW, respectively, corresponding to arc-to-target efficiencies of 64% and 32%, respectively. The averaged fluxes measured are 1.4 MW m^{-2} and 0.7 MW m^{-2}. Simulations of the flux distribution on a virtual sphere behind the focal plane, reported by Bader et al. [9], confirm that “hot spots” are reduced.

Optics EXPRESS

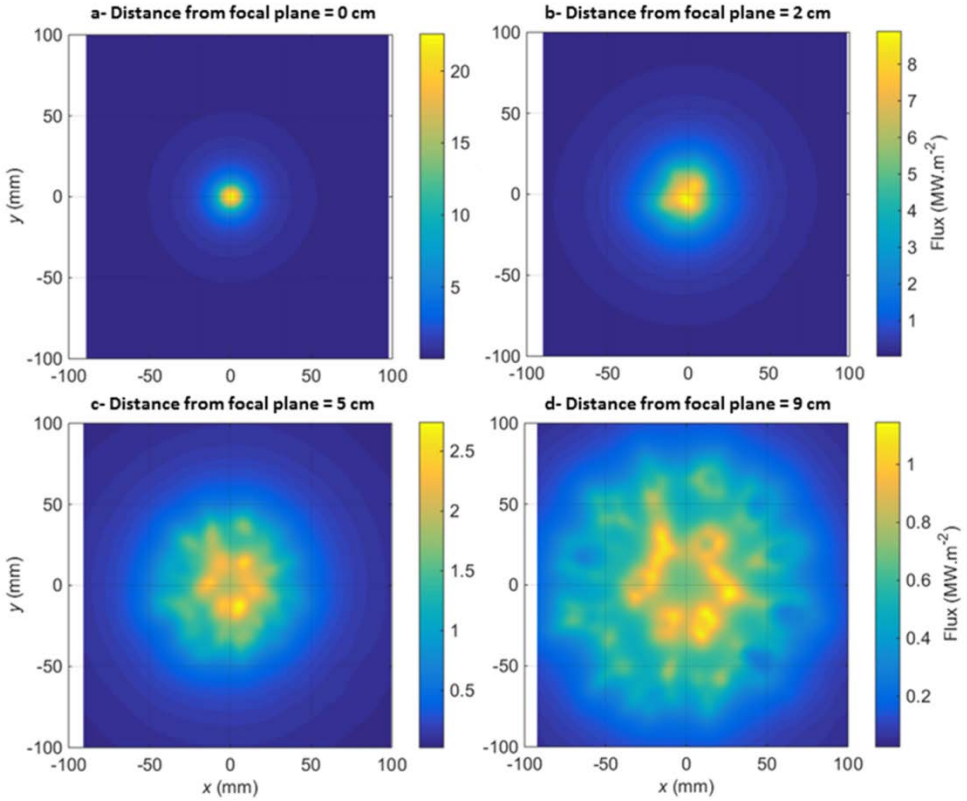

Fig. 6. Flux maps measured at the focal plane (a), and in planes at 2, 5, and 9 cm behind the focal plane (b-d). Peak fluxes measured are 21.67 MW m^{-2} in the focal plane, 8.89 MW m^{-2} in the plane 2 cm behin the focal plane, 2.74 MW m^{-2} in the plane 5 cm behin the focal plane, and 1.14 MW m^{-2} in the plane 9 cm behin the focal plane.

3.6. Numerical results

3.6.1. Simulation calibration

The results of the simulation calibration are shown in Figs. 7 and 8. The best-fit values for the unknown model parameters are listed in Table 2 along with the goodness-of-fit parameters. The lamp efficiency is in good agreement with the value of 42% reported in [23] for a 150 W Xe short-arc lamp. The remainder of the electric power input to the lamp is dissipated via thermal radiation from the electrodes and convection from the hot surfaces of the lamp. The best-fit surface error for these electroformed reflectors, determined to be 0.85 mrad, is significantly lower than the value of 2.5 mrad determined previously for spin-formed reflectors [24]. This confirms the visual impression of the superior reflector surface quality obtained with electroforming compared to spin forming. For comparison, the ray-tracing simulation is repeated with a surface error of 2.5 mrad instead of 0.85 mrad, with all other parameters unchanged. This reduces the peak flux from 20.8 MW m^{-2} to 8.3 MW m^{-2}.

Since all rays that reach the focal plane undergo exactly one reflection on the reflector, the determined value for the lamp efficiency is inversely proportional to the choice of the reflectivity of the reflectors.

Optics EXPRESS

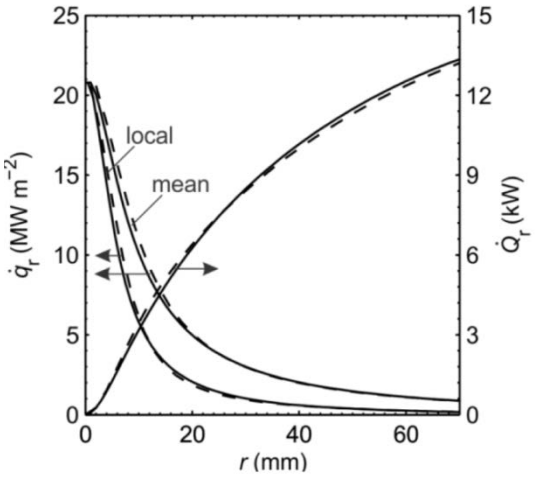

Fig. 7. Comparison of measured (dashed lines) and simulated (solid lines) radial profiles of the local and mean radiative flux, and radiative power, as a function of the radial coordinate, *r*, from the center of the focal plane, for the best-fit simulation parameters listed in Table 2.

Table 2. Results of the simulation calibration.

Best-fit model parameters	
η_{lamp} , %	39.4
θ_{m} , mrad	0.85
C_1	1.7
Goodness-of-fit parameters	
$\varepsilon_{\text{peak}}$, %	4.2%
R_{local}	0.9990
R_{mean}	0.9995

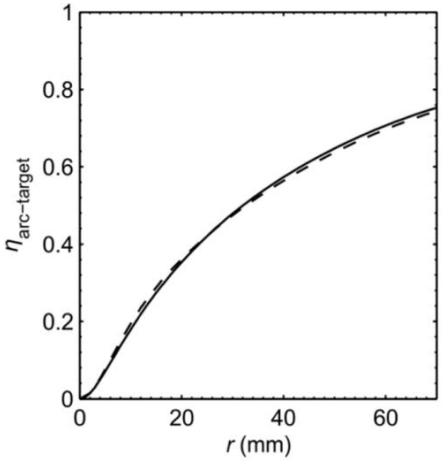

Fig. 8. Optical efficiency of the setup (solid line: simulated, dashed line: measured) as a function of the radial coordinate, *r*, from the center of the focal plane, for the best-fit simulation parameters listed in Table 2.

Optics EXPRESS

3.6.2. Flux homogeneity in off-focal planes

Figure 9 presents the simulated flux distributions obtained on planes at 0, 2, 5, and 9 cm behind the focal plane with all 18 lamps in operation, for comparison with the experimental results presented in Fig. 6. Overall, the patterns observed in the simulated and measured flux distributions are in good agreement.

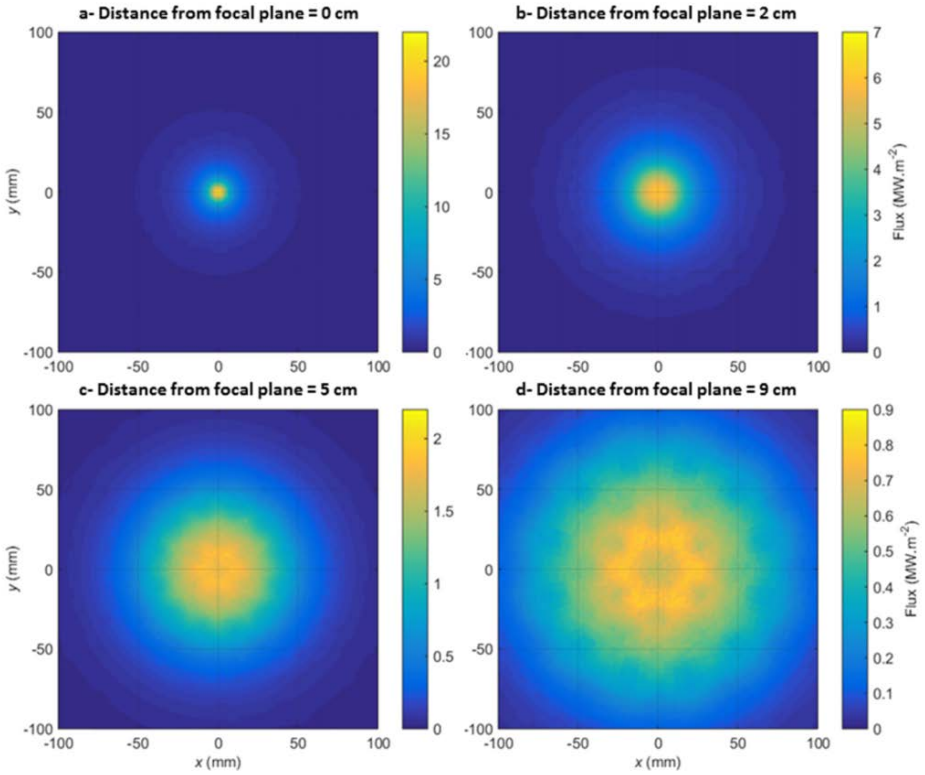

Fig. 9. Numerical results obtained at the focal plane (a), and in planes at 2, 5, and 9 cm behind the focal plane (b-d).

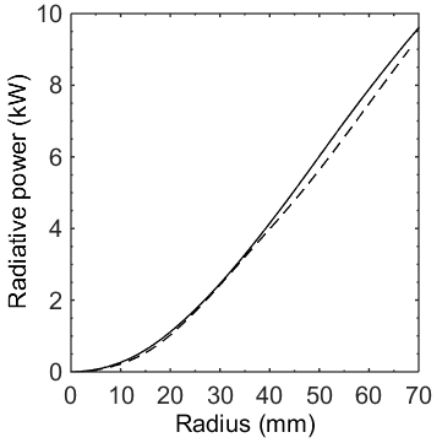

Fig. 10. Measured (dashed line) and simulated (solid line) radial profiles of the integrated radiative power at 9 cm from the focal plane.

Optics EXPRESS

The measured flux distribution shows some irregularities that constitute flux peaks ("hot spots"), which are not predicted by the model and are associated to non-perfect mirror shapes and positioning of the light source relatively to the first focus point (see 3.1 and 3.4). Despite these local differences, the integrated radiative power at a given radius from the center of the flux distribution obtained with the model are very similar to the measured values (Fig. 10).

4. Conclusion

A new 45 kW HFSS was successfully calibrated and characterized. The presented results were obtained following a method using a CCD camera and a Lambertian target, whose reliability had been proven in previous studies. The basic assumptions of the approach, i.e. additivity of flux maps, correctness of flux gauge calibration, spatial uniformity of HFSS spectrum and CCD chip response, and linearity of CCD chip response, were investigated and proven correct for the studied setup and measurement aparatus. The main source of uncertainty was identified to be the flux gauge with an estimated uncertainty of 10% of the measured value.

Measured peak flux was 1.0–1.5 ± 0.1 MW m^{-2} per lamp and 21.7 MW m^{-2} with all 18 lamps in operation. For a practically relevant target area of 50 mm diameter, an average flux of 3.8 MW m^{-2} was obtained, corresponding to 7.5 kW of radiative power. The measured arc-to-target radiation transfer efficiency was 42%. Moving 9 cm away from the focal plane, peak and average flux were measured at 1.2 MW m^{-2} and 0.7 MW m^{-2}, corresponding to a radiative power of 5.7 kW.

The experimental results were used to refine a Monte Carlo ray-tracing model of the system. The optimal values for the unknown parameters are a lamp electricity-to-arc efficiency of 39.4%, in good agreement with reported values, and a specular error of 0.85 mrad, which emphasizes the good quality of the mirror surface obtained by electroforming.

Finally, an important feature of this HFSS design is its versatility in power and flux distributions achievable, thanks to the possibility of selecting power, flux, and incidence angle by choosing the number of radiation modules in operation, the electric current input to the lamp, the distance from the focal plane, and by selecting different combinations of radiation modules. This adaptability of the radiative source in addition to the flux values reported ensures a very large area of applications, including CPV stress tests (a few hundreds of sun, collimated irradiation), solar receiver/reactor operation (thousands of suns), applied radiative heat transfer research and extreme condition material testing.

Acknowledgments

The authors thank Lutz Schmidt, Jörg Röschenthaler and the engineering team from Kinoton Digital Solutions GmbH, Jean-Marc Schwab and Meng Lin from EPFL, and Dr Jason Chen and Colin Carvolth from the Australian National University for their contributions to the development of the presented high-flux solar simulator facilities.